

Cite this: *Chem. Sci.*, 2025, 16, 16801

All publication charges for this article have been paid for by the Royal Society of Chemistry

A leveling–shielding dual strategy enabling stable zinc anodes to exhibit ultra-low interfacial impedance

Qing Wen,^{abc} Taixu Hao,^a Tian Chen,^{abc} Dinghao Le,^{abc} Pei Yang,^{abc} Hezhang Chen,^{id} Linbo Tang,^e Qing Wu,^f Xiahui Zhang,^{id} *^{abc} and Junchao Zheng,^{id} *^{abc}

Aqueous zinc-ion batteries have demonstrated great potential for large-scale energy storage, but still suffer from severe dendrites and corrosion problems. Uneven distributions of crystalline planes and passivation layers on the zinc anode are the key factors causing dendrites and corrosion. However, the synergistic construction of uniform crystal planes and shielding layers is still challenging. Herein, we propose a novel leveling–shielding dual strategy to stabilize the zinc anode. The low-melting-point indium (In) layer not only serves as a leveling agent to repair surface defects, but also induces uniform and fast deposition of zinc by exposing a single (101)_{In} plane on the anode. Besides, the outer ZnF₂ shielding layer can inhibit corrosion and accelerate the de-solvation of Zn(H₂O)₆²⁺, which improves the electrochemical reaction kinetics. As a result, the ZnF₂@In@Zn symmetric cell shows an ultra-low interfacial impedance of <10 Ω and a stable cycle life of >2800 h with a low polarization voltage of 21.8 mV at 5 mA cm⁻² and 2 mAh cm⁻², compared with bare Zn (140 h and 75.8 mV). Besides, the ZnF₂@In@Zn//NH₄V₄O₁₀ full cell maintains a high capacity of 112.4 mAh g⁻¹ with a retention rate of 79.5% after 10 000 cycles at 3 A g⁻¹. This work provides a novel, effective leveling–shielding dual strategy for interfacial modification of zinc anodes, which can also be applied in other metal anodes.

Received 2nd July 2025

Accepted 12th August 2025

DOI: 10.1039/d5sc04875c

rsc.li/chemical-science

1 Introduction

During the critical stage of global energy structure transformation, energy security has become a core issue for the sustainable development of human civilization.^{1,2} Currently, fossil fuels still dominate the global primary energy consumption structure (accounting for 79.6%), and 73.2% of the greenhouse gas emissions stem from energy activities.³ While clean energy technologies like photovoltaics and wind power can reduce carbon emission intensity by over 90%, their inherent geographical unevenness and intermittent nature necessitate supporting energy storage systems for stable power output.^{4–6} Among existing energy storage technologies, lithium-ion batteries are subject to high costs and thermal runaway risks,

which hinder their ability to meet large-scale storage needs;⁷ pumped storage, though economical, demands strict geographical conditions (requiring elevation drops exceeding 400 m).⁸ Thanks to high volumetric energy density (5850 mAh cm⁻³), cost-effectiveness, and inherent non-flammability, aqueous zinc ion batteries have emerged as promising candidates for large-scale energy storage.^{9–12} However, uncontrolled dendrite growth and interfacial side reactions of the zinc anode during cycling degrade battery cycle stability, thereby restricting industrial application.^{13–15}

The uneven distribution of crystal planes and passivation layers (such as Zn₂(OH)₂CO₃ and ZnO) on the zinc anode is a key factor leading to zinc dendrites and corrosion. Various crystal planes, including (002)_{Zn}, (100)_{Zn} and (101)_{Zn}, are randomly distributed on the initial zinc anode. Due to differences in the adsorption energy of zinc on different crystal planes, the zinc anode exhibits uneven zinc deposition dynamics across various regions.¹⁶ Meanwhile, the corrosion potentials of different crystal planes vary, leading to the uneven distribution of corrosion and passivation layers.^{17,18} These differences in deposition dynamics and the uneven distribution of corrosion and passivation layers synergistically accelerate dendrite growth. Additionally, owing to the low overpotential of zinc (−0.76 V vs. the Hydrogen Evolution Reaction (HER)), prolonged corrosion is thermodynamically inevitable in weakly acidic electrolyte (Fig. 1a). Among numerous modification strategies,

^aSchool of Metallurgy and Environment, Central South University, Changsha 410083, China. E-mail: xhzhang@csu.edu.cn; jczheng@csu.edu.cn

^bEngineering Research Center of the Ministry of Education for Advanced Battery Materials, Central South University, Changsha 410083, China

^cNational Energy Metal Resources and New Materials Key Laboratory, Central South University, Changsha 410083, China

^dSchool of Chemistry and Chemical Engineering, Hunan University of Science and Technology, Xiangtan 411201, China

^eSchool of Materials and Environmental Engineering, Changsha University, Changsha, Hunan, 410022, China

^fSchool of Information and Network Center Central South University, Changsha 410083, China



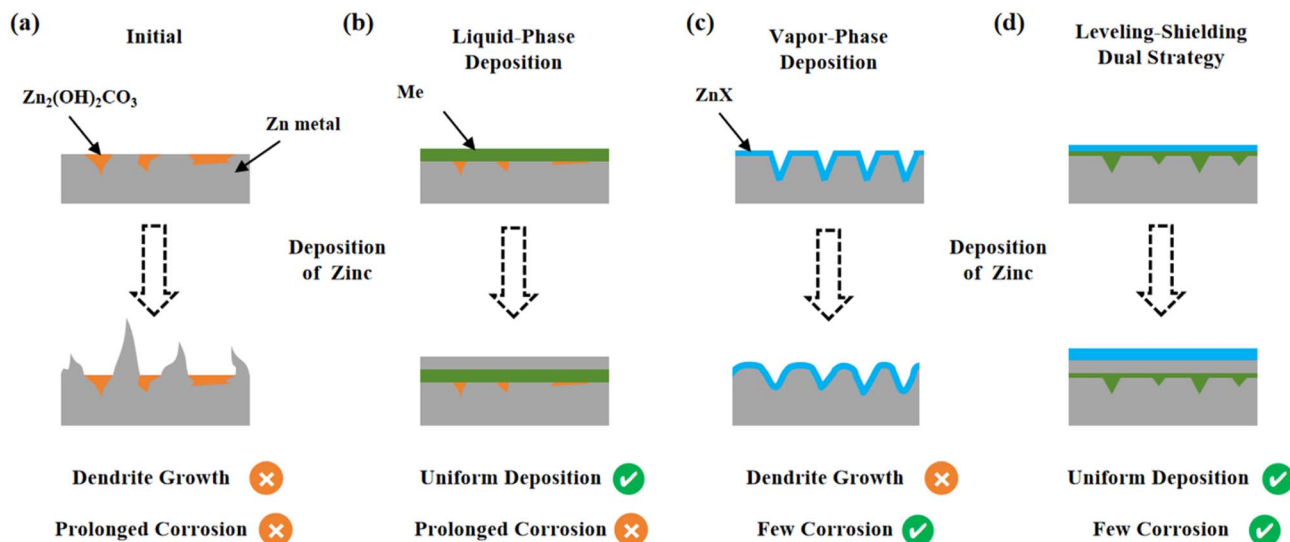


Fig. 1 Schematic illustration of dendrite growth and corrosion at the modified interface. (a) Bare Zn, (b) metal modified layer by liquid-phase deposition, (c) metal compound modified layer by vapor-phase deposition and (d) metal and metal compound composite layer by a leveling-shielding dual strategy.

such as using electrolyte additives,^{19,20} high-concentration electrolytes,^{21,22} and hydrogel electrolytes,^{23,24} significant progress has been achieved in mitigating dendrite formation and corrosion. However, these approaches have exhibited limited efficacy in addressing the uneven distributions of crystal planes and passivation layers on the anode. Interfacial modification, which can improve the surface properties of the anode, has garnered substantial research attention and is considered a promising strategy to solve these challenges.^{25,26}

Commonly used interface modification methods can be categorized into physical coating, liquid-phase deposition, and vapor-phase deposition. Physical coating relies on adhesive bonding with the anode, which struggles to achieve molecular-level coverage and offers limited enhancement to the properties of initial zinc.²⁶ In contrast, liquid-phase and vapor-phase deposition are *in situ* growth methods requiring chemical reactions with zinc metal, which can improve the surface properties of initial zinc. For instance, some high-potential metals (such as In,²⁷ Cu²⁸ and Sn²⁹) can replace zinc through liquid-phase deposition to form a metal modification layer on the zinc anode. The specific crystal planes of these metals facilitate uniform zinc deposition (Fig. 1b). However, the corrosion issue of deposited zinc remains unsolved. Depositing metal compounds (such as ZnF_2 ,^{30–32} ZnSe ³³ and ZnS ³³) with high ionic conductivity on the anode through vapor-phase deposition can hinder the contact between the deposited zinc and the electrolyte, thereby inhibiting the prolonged corrosion of zinc (Fig. 1c). However, the decomposition of $\text{Zn}_2(\text{OH})_2\text{CO}_3$ results in holes on the anode during vapor-phase deposition, which is detrimental to uniform deposition. Additionally, the uneven distribution of zinc crystal planes within the coating layer still poses the risk of dendrite growth. Therefore, it is urgent to develop a modified layer with uniformly distributed crystal planes and passivation layers to simultaneously inhibit dendrites and corrosion.

Herein, we propose a leveling-shielding dual strategy to construct a stable Zn anode (Fig. 1d). The low-melting-point In metal serves as a leveling agent to repair surface defects caused by the decomposition of $\text{Zn}_2(\text{OH})_2\text{CO}_3$ during heat treatment. The exposed single $(101)_{\text{In}}$ plane can induce uniform and rapid deposition of zinc. The outermost ZnF_2 shielding layer can inhibit the corrosion of deposited zinc and accelerate the dissolution process of $\text{Zn}(\text{H}_2\text{O})_6^{2+}$, which further improves the electrochemical reaction kinetics. As a result, the $\text{ZnF}_2@\text{In}@\text{Zn}$ symmetric cell demonstrates an ultra-low interfacial impedance of less than 10Ω and achieves stable cycling for over 2800 h with a polarization voltage of 21.8 mV at 5 mA cm^{-2} and 2 mAh cm^{-2} , a significant improvement over that of bare Zn (140 h, 75.8 mV). Additionally, the $\text{ZnF}_2@\text{In}@\text{Zn}/\text{NH}_4\text{V}_4\text{O}_{10}$ full cell retains a capacity of 112.4 mAh g^{-1} after 10 000 cycles at 3 A g^{-1} , corresponding to a capacity retention rate of 79.5%.

2 Results and discussion

The leveling-shielding dual strategy involves two stages of *in situ* deposition: the In metal layer is constructed through liquid-phase deposition and the ZnF_2 layer is constructed by vapor-phase deposition (Fig. 2a). Based on the Zn–In binary metal phase diagram (Fig. S1), during vapor-phase deposition, the In metal and surface Zn metal undergo eutectic melting to form a homogeneous melt. Given that Zn has a lower potential than In, HF produced by the decomposition of NH_4F selectively reacts with Zn to produce ZnF_2 , which deposits on the surface. As cooling begins, Zn preferentially precipitates from the melt with the formation of grain boundaries. With further cooling, the ZnIn alloy can infiltrate into the grain boundaries and holes, precipitating within them and effectively healing surface defects. The reactions involved in this entire process are as follows:



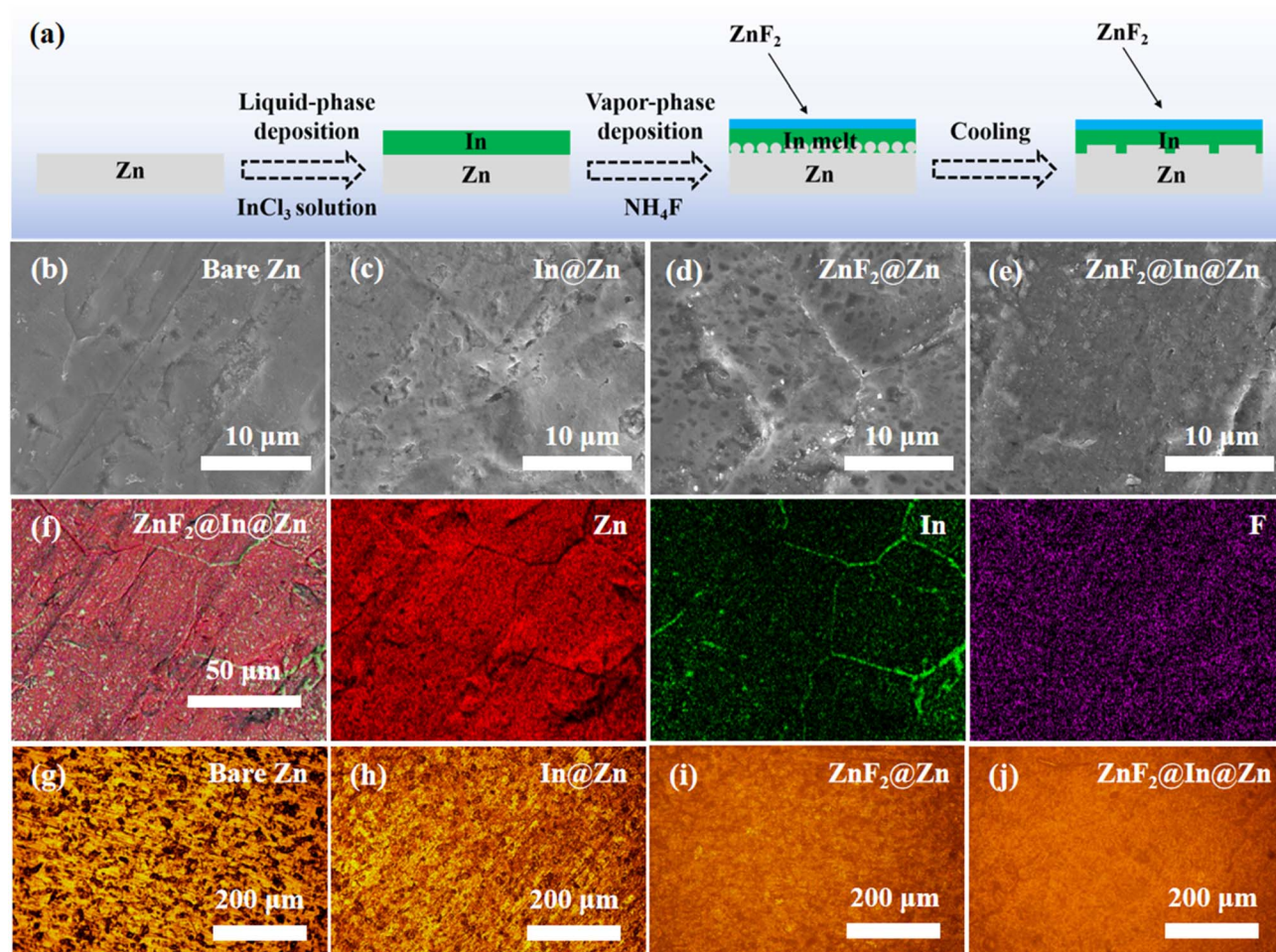
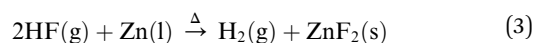
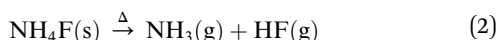


Fig. 2 Surface morphology analysis of various anodes. (a) Schematic diagram of the preparation of a $\text{ZnF}_2@\text{In}@\text{Zn}$ anode by the leveling-shielding dual strategy. SEM images of (b) bare Zn, (c) $\text{In}@\text{Zn}$, (d) $\text{ZnF}_2@\text{Zn}$ and (e) $\text{ZnF}_2@\text{In}@\text{Zn}$. (f) Mapping images of $\text{ZnF}_2@\text{In}@\text{Zn}$. Metallographic microscope image of (g) bare Zn, (h) $\text{In}@\text{Zn}$, (i) $\text{ZnF}_2@\text{Zn}$ and (j) $\text{ZnF}_2@\text{In}@\text{Zn}$.



Scanning electron microscopy (SEM) reveals the morphological evolution during the construction of the $\text{ZnF}_2@\text{In}@\text{Zn}$ anode. The initial zinc surface is smooth and flat (Fig. 2b and S2a). After liquid-phase deposition, the surface morphology of the $\text{In}@\text{Zn}$ anode remains largely unchanged, possibly due to the strong binding energy between In and Zn, which allows In to be embedded within the Zn lattice to form a ZnIn alloy (Fig. 2c and S2b). In the absence of In, tiny holes emerge on the surface of $\text{ZnF}_2@\text{Zn}$ (Fig. 2d and S2c). In contrast, the $\text{ZnF}_2@\text{In}@\text{Zn}$ anode maintains a relatively flat surface (Fig. 2e and S2d). Compared to $\text{ZnF}_2@\text{Zn}$, the heat-treated Zn exhibits larger and denser holes in the Ar atmospheres (Fig. S2e and f). This indicates that the holes are formed by the decomposition of $\text{Zn}_2(\text{OH})_2\text{CO}_3$ on the zinc surface. Notably, the ZnF_2 produced by vapor-phase deposition

can partially fill these holes. The mapping diagram illustrates the distribution of elements. The surface of bare Zn is covered with C, O, and Zn elements, and EDS also detected a certain amount of C and O elements, indicating the presence of $\text{Zn}_2(\text{OH})_2\text{CO}_3$ on the bare Zn surface (Fig. S3). In both the $\text{In}@\text{Zn}$ and $\text{ZnF}_2@\text{Zn}$ anodes, elements are uniformly distributed, indicating an even modification layer on the zinc surface (Fig. S4). For the $\text{ZnF}_2@\text{In}@\text{Zn}$ anode, F and Zn elements are also evenly distributed, showing that the ZnF_2 layer is uniformly constructed (Fig. 2f). However, In distribution on the $\text{ZnF}_2@\text{In}@\text{Zn}$ surface is localized in spots and lines (Fig. 2f). This suggests that during cooling, In metal fills the grain boundaries and pores of zinc, repairing surface defects. Besides, the $\text{ZnF}_2@\text{In}@\text{Zn}$ anode exhibits a distinct trilayer structure. Layer A is a ZnF_2 layer, layer B mainly consists of In, and layer C is primarily composed of Zn. The thickness of the ZnF_2 layer is approximately $6.8 \mu\text{m}$ and the thickness of the In layer is about $1 \mu\text{m}$ (Fig. S5). As shown in the In element distribution mapping, In metal tends to concentrate in the depressions. This further confirms that In metal fills the grain boundaries and pores of zinc. The metallographic microscope image reveals the occurrence form of metals on the surface. The



inert passivation layer appears black due to its low reflectivity, whereas metals with high reflectivity exhibit a bright golden color. On the bare Zn surface, bright golden and black spots are randomly distributed, indicating an uneven passivation layer

(Fig. 2g). For the In@Zn anode, the black spots are reduced, yet the color distribution remains non-uniform, suggesting that some passivation layer exists (Fig. 2h). Thanks to the uniform

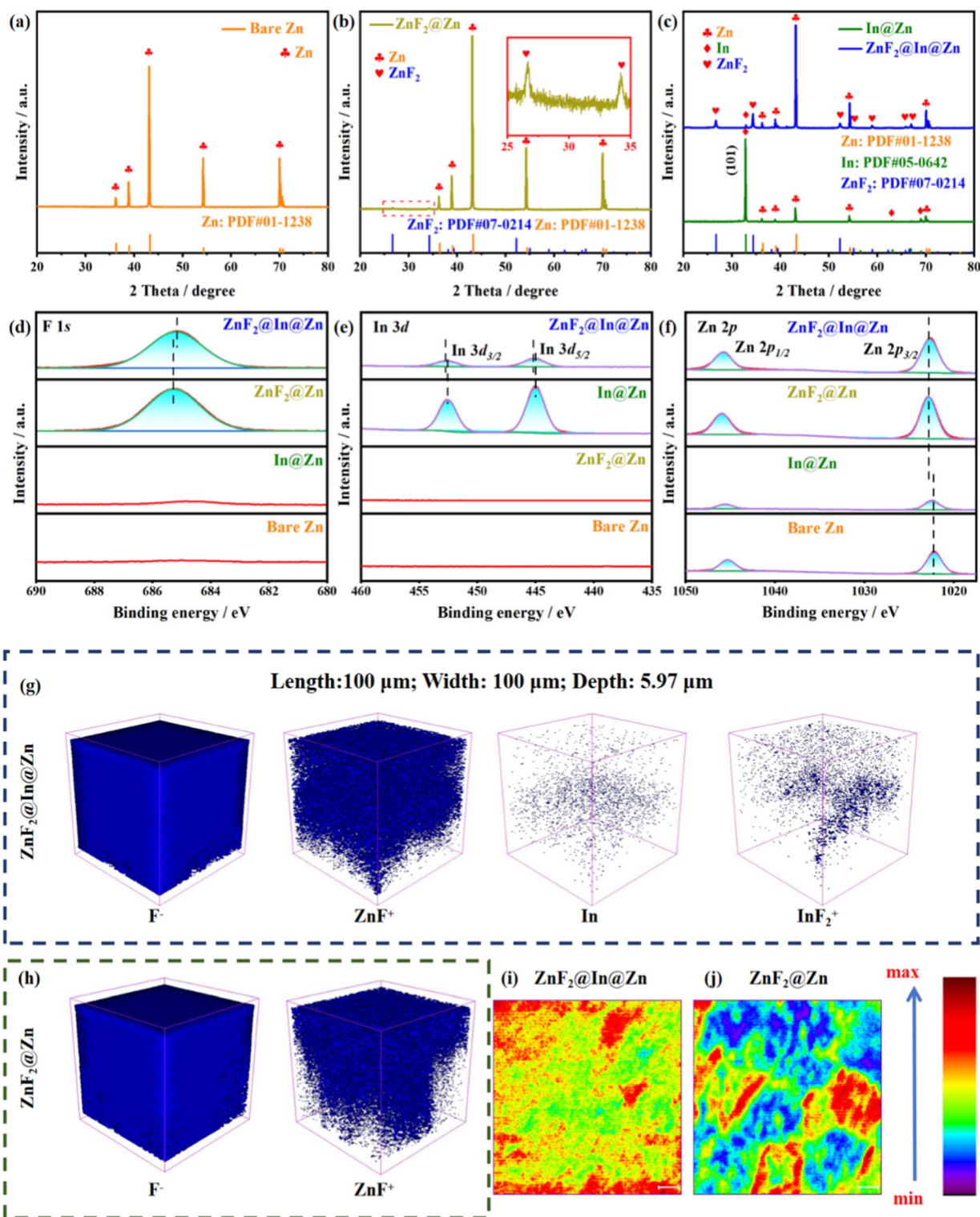


Fig. 3 Study of element distribution on various anode surfaces. XRD spectra of (a) bare Zn, (b) $\text{ZnF}_2@Zn$, (c) $\text{In}@Zn$ and $\text{ZnF}_2@In@Zn$. High-resolution (d) F 1s, (e) In 3d and (f) Zn 2p XPS spectra. TOF-SIMS images of (g) $\text{ZnF}_2@In@Zn$ and (h) $\text{ZnF}_2@Zn$. ZnF^+ signal intensity of (i) $\text{ZnF}_2@In@Zn$ and (j) $\text{ZnF}_2@Zn$ (length: 100 μm ; width: 100 μm ; depth: 5.97 μm).



distribution of ZnF₂, the ZnF₂@Zn and ZnF₂@In@Zn anodes show a uniform orange-yellow color (Fig. 2i and j).

X-ray diffraction (XRD) and X-ray photoelectron spectroscopy (XPS) reveal the surface material composition. The XRD pattern of bare Zn corresponds well with the standard spectrum (PDF #01-1238) (Fig. 3a). A weak peak attributable to ZnF₂, in accordance with PDF #07-0214, is present in the diffraction profile of the ZnF₂@Zn anode (Fig. 3b). For the In@Zn anode, an intense indium peak at 33°, linked to the (101) plane and consistent with PDF #05-0642, is observed. This indicates substantial exposure of the (101)_{In} plane on the anode surface (Fig. 3c). Compared with the ZnF₂@Zn anode, the ZnF₂@In@Zn anode exhibits a more pronounced ZnF₂ peak, suggesting that the melt facilitates the fluorination reaction (Fig. 3c). Additionally, the ZnF₂@In@Zn anode shows a reduced In peak intensity, with only the (101)_{In} plane detectable, which could be attributed to the ZnF₂ layer partially shielding the In signal (Fig. 3c). It is worth noting that the ZnF₂@In@Zn anode displays a higher $I_{(101)Zn}/(I_{(002)Zn} + I_{(100)Zn})$ peak intensity ratio (~6.87) compared to bare Zn (~3.99) (Fig. S6a). Conversely, the In@Zn and ZnF₂@Zn anodes exhibit lower ratios than bare Zn (Fig. S6b). This implies that the replacement and fluorination processes do not enhance the exposure of the (101)_{Zn} plane. The increased exposure of the (101)_{Zn} plane on the ZnF₂@In@Zn anode may result from the recrystallization of the Zn–In melt along the (101) plane. The full XPS spectrum detects Zn, F, and In peaks on the ZnF₂@In@Zn anode (Fig. S7). The Cl peak is found at the In@Zn anode, attributed to residual Cl from the InCl₃ solution (Fig. S7). In the high-resolution F 1s XPS spectrum, the F peak in ZnF₂@In@Zn is right-shifted relative to ZnF₂@Zn (Fig. 3d), likely due to the binding of some of the In and F. The high-resolution In 3d XPS spectrum shows that the In peak in ZnF₂@In@Zn is left-shifted compared to In@Zn (Fig. 3e), further indicating the binding of In and F. In the high-resolution Zn 2p XPS spectrum, ZnF₂@In@Zn and ZnF₂@Zn show left-shifted peaks compared to bare Zn and In@Zn (Fig. 3f), which is because the binding energy between Zn and F is stronger than that between Zn and O.

Time-of-flight secondary ion mass spectrometry (TOF-SIMS) offers a more intuitive analysis of the elemental distribution on the surfaces of the ZnF₂@Zn and ZnF₂@In@Zn anodes. Both anode surfaces are densely covered with F[−] and ZnF⁺ signals, indicating complete coverage of the outermost layer by ZnF₂ (Fig. 3g and h). In the ZnF₂@In@Zn anode, the weak In signal suggests that the In layer is enveloped by the ZnF₂ layer, which can suppress the corrosion of deposited zinc. Furthermore, the detection of InF₂⁺ signals in the ZnF₂@In@Zn anode provides additional evidence of In–F bonding (Fig. 3g). The intensity of the ZnF⁺ signal on the ZnF₂@In@Zn anode is stronger and more uniform than that on the ZnF₂@Zn anode (Fig. 3i and j). This may be because the melt accelerates the fluorination reaction, enhancing its completeness, and exhibits good wettability, allowing it to spread evenly across the anode surface.

Benefiting from its surface defect repair and the abundant coverage of ZnF₂, the ZnF₂@In@Zn anode demonstrates ultra-fast electrochemical kinetics, achieving polarization voltages of

7.2, 10.9, 14.6, 21.8, and 38 mV at current densities of 1, 2, 3, 5, and 10 mA cm^{−2}, respectively (Fig. 4a, c and S8). Similarly, ZnF₂@Zn (22.4, 25.9, 29.7, 38.8, and 59.8 mV) and In@Zn anodes (12.5, 18.9, 23.9, 34.4, and 58.2 mV) exhibit comparatively low polarization voltages at the same current densities (Fig. 4b, c and S8). In contrast, bare Zn shows significantly highest polarization voltages of 41.6, 53, 62, 75.8, and 96.9 mV at these current densities (Fig. 4a, c and S8). This difference is attributed to interfacial corrosion and dendrite issues in bare Zn. Moreover, ZnF₂@In@Zn has a much lower nucleation overpotential of 4.2 mV compared to bare Zn (108.6 mV), In@Zn (36.5 mV), and ZnF₂@Zn (32.4 mV) (Fig. 4d, e and S9). This indicates a faster zinc nucleation process and a higher zinc nucleation density for the ZnF₂@In@Zn anode. Moreover, compared with bare Zn, the ZnF₂@In@Zn anode exhibits superior wettability with electrolytes, which is beneficial for reducing polarization voltage and nucleation overpotential (Fig. S10). To more accurately evaluate the deposition kinetics, we calculated the exchange current density during zinc deposition. As shown in Fig. S11a, bare Zn has a low exchange current density of only 8.7 mA cm^{−2}, whereas ZnF₂@In@Zn has a significantly higher value of 14.6 mA cm^{−2}, indicating faster deposition kinetics. Additionally, In@Zn and ZnF₂@Zn also exhibit increased exchange current densities compared to bare Zn, demonstrating that both the In layer and the ZnF₂ layer can enhance the deposition kinetics (Fig. S11b).

To evaluate the corrosion resistance of ZnF₂@In@Zn, electrochemical impedance spectroscopy (EIS) is conducted at various resting times. Fig. S12 presents the equivalent circuit diagram, and Table S1 lists the values of solution resistance (*R*_s), solid electrolyte interfacial impedance (*R*_{EIS}), and charge transfer impedance (*R*_{ct}) for various anodes at different resting times. As the resting time increased, bare Zn exhibited a continuous rise in both *R*_{EIS} and *R*_{ct}, indicative of ongoing corrosion (Fig. 4f). During the resting period, In@Zn showed fluctuations in *R*_{EIS} and *R*_{ct}, likely due to temperature variations in the testing environment (Fig. S13a). However, overall, the In@Zn anode maintained extremely low *R*_{EIS} and *R*_{ct}, highlighting superior corrosion resistance and electronic transport properties of In. The ZnF₂@Zn anode experienced a gradual increase in *R*_{EIS} and *R*_{ct}, possibly due to electrolyte penetration through surface pores (Fig. S13b). Nonetheless, its impedance remained significantly lower than that of bare Zn. Benefiting from In's role in repairing interfacial defects, ZnF₂@In@Zn demonstrated the lowest and most stable *R*_{EIS} and *R*_{ct} of less than 10 Ω (Fig. 4g). This underscores its rapid electrochemical kinetics and excellent corrosion resistance. It is also worth noting that *R*_{EIS} and *R*_{ct} of In@Zn are marginally higher than those of ZnF₂@In@Zn. This slight discrepancy may stem from partial oxidation of In metal during storage and construction. Furthermore, the ZnF₂@In@Zn anode similarly demonstrates low polarization voltage and low charge transfer impedance at high current densities compared to other studies on anode modification (Fig. 4h). To further assess the ability of the ZnF₂@In@Zn anode to suppress interfacial side reactions, linear sweep voltammetry (LSV) curves of bare Zn and ZnF₂@In@Zn anode were measured. Compared with bare Zn (−1.83 V), the



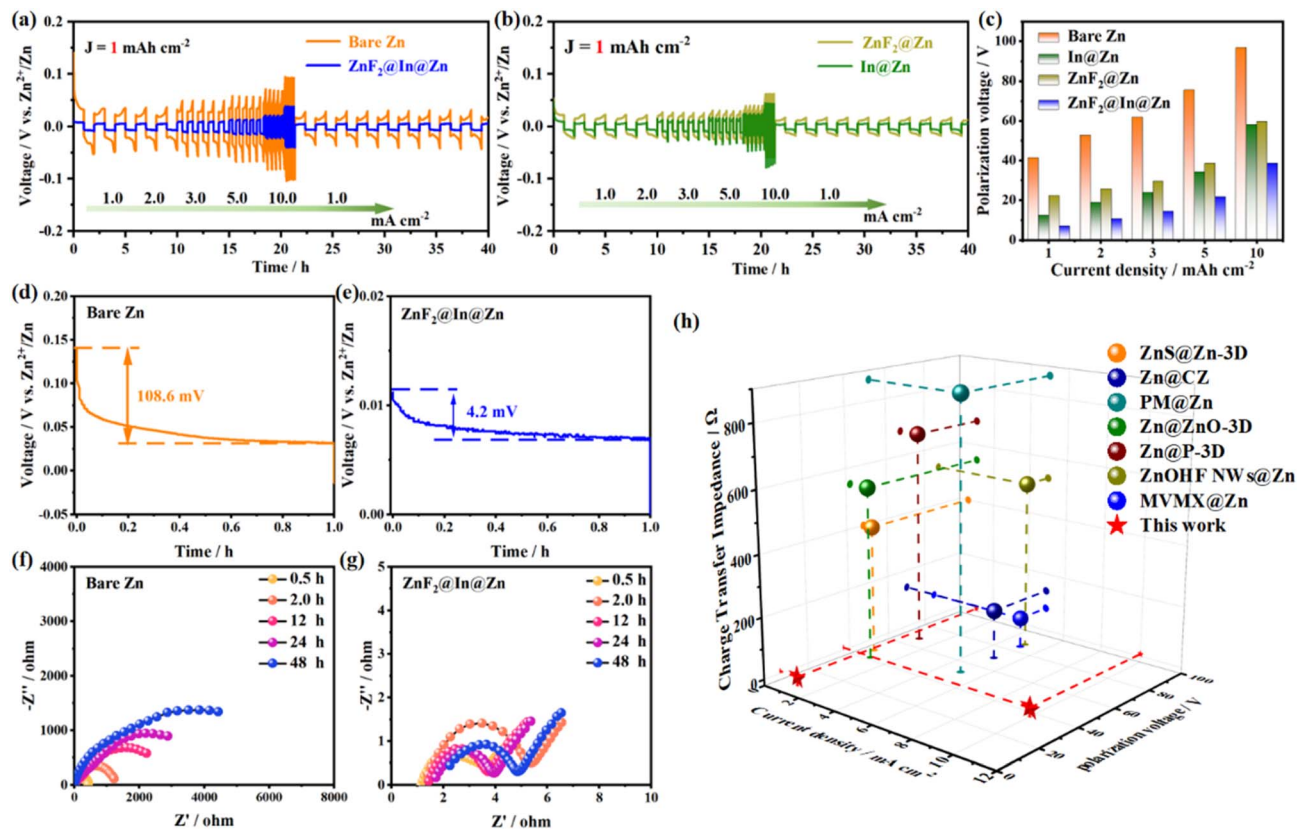


Fig. 4 Study of kinetic processes in symmetric cells. Multiplication performance of symmetric cells assembled with (a) bare Zn, $\text{ZnF}_2@In@Zn$, (b) $In@Zn$ and $\text{ZnF}_2@Zn$ anodes. (c) Polarization voltage histograms of various anodes at different current densities. Voltage–time plots of symmetric cells assembled with (d) bare Zn and (e) $\text{ZnF}_2@In@Zn$. EIS of symmetric cells assembled from (f) bare Zn and (g) $\text{ZnF}_2@In@Zn$ anode at various resting times. (h) Comparison of this work with published studies in terms of current density, polarization voltage and charge transfer impedance.^{34–40}

$\text{ZnF}_2@In@Zn$ anode has a lower hydrogen evolution overpotential of -2.01 V (vs. $Ag/AgCl$) (Fig. S14). This indicates that the $\text{ZnF}_2@In$ layer effectively suppresses the hydrogen evolution reaction.

The cycle life of $\text{ZnF}_2@In@Zn$ symmetric cells was further evaluated. Under $1\text{ mA cm}^{-2}/1\text{ mAh cm}^{-2}$ conditions, the $\text{ZnF}_2@In@Zn$ anode demonstrates stable cycling for over 4000 h, a significant improvement over bare Zn, which fails after only 350 h (Fig. S15). When the current density and deposition amount are increased to $5\text{ mA cm}^{-2}/2\text{ mAh cm}^{-2}$, the $\text{ZnF}_2@In@Zn$ anode maintains a cycle life exceeding 2800 h, whereas bare Zn survives only for 140 h (Fig. 5a). Under more demanding conditions of $10\text{ mA cm}^{-2}/5\text{ mAh cm}^{-2}$, the $\text{ZnF}_2@In@Zn$ anode achieves a cycle life of over 500 h with a low polarization voltage of 37 mV, whereas bare Zn fails after 41 h with a polarization voltage of 79 mV (Fig. 5b). Additionally, under $10\text{ mA cm}^{-2}/5\text{ mAh cm}^{-2}$ conditions, $\text{ZnF}_2@Zn$ and $In@Zn$ anodes also show extended cycle lives of 344 and 100 h (Fig. S16), respectively, compared to bare Zn. This shows that a single protective layer can also improve the cycle stability of the anode. Moreover, the $\text{ZnF}_2@In@Zn$ anode demonstrates superior cycling stability at various rates compared to other reported studies (Fig. 5c).

Lower polarisation voltage is closely related to deposition kinetics. In general, zinc deposition can be divided into four processes: (1) diffusion of $\text{Zn}(\text{H}_2\text{O})_6^{2+}$ to the anode surface; (2) de-solvation of $\text{Zn}(\text{H}_2\text{O})_6^{2+}$; (3) transport of Zn^{2+} from the passivation layer to the surface of the metal layer; (4) the electrical crystallisation. The diffusion of $\text{Zn}(\text{H}_2\text{O})_6^{2+}$ to the anode surface is usually consistent as the electrolyte composition remains unchanged. To investigate the effect of bare Zn and $\text{ZnF}_2@In@Zn$ on the de-solvation of $\text{Zn}(\text{H}_2\text{O})_6^{2+}$, the EIS of the symmetric cell was obtained at different temperatures. As the temperature increases, the R_{ct} and R_{SEI} of the bare Zn symmetric battery drop sharply (Fig. S18a), whereas those of the $\text{ZnF}_2@In@Zn$ symmetric battery decrease only slightly (Fig. 5d). The activation energies for the two impedances of the $\text{ZnF}_2@In@Zn$ anode, calculated *via* the Arrhenius equation based on R_{ct} and R_{SEI} at different temperatures, are lower than those of the bare Zn, indicating faster de-solvation of $\text{Zn}(\text{H}_2\text{O})_6^{2+}$ (Fig. 5e and S18b). Additionally, ZnF_2 exhibits a higher binding energy for Zn^{2+} (-21.8 eV) compared to H_2O (-4.8 eV), indicating its ability to accelerate the de-solvation of $\text{Zn}(\text{H}_2\text{O})_6^{2+}$ (Fig. 5f). To evaluate Zn^{2+} transport in the passivation layer, the ionic transference numbers of the bare Zn and $\text{ZnF}_2@In@Zn$ anodes were tested and calculated. Compared to bare Zn (0.16), the $\text{ZnF}_2@In@Zn$ anode has a higher Zn^{2+} transference number (0.72), showing



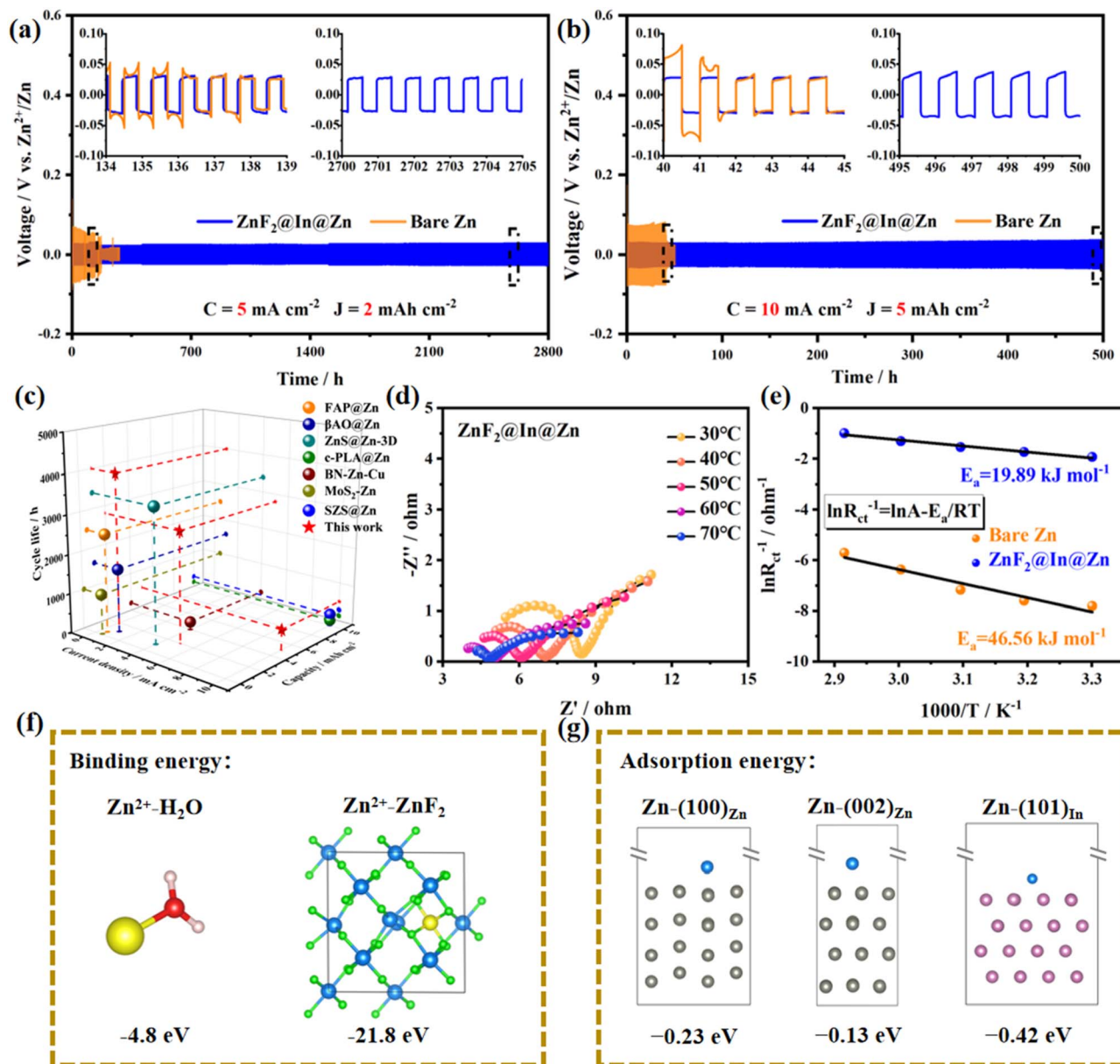


Fig. 5 Study of cycling stability in symmetric cells. Cycling performance test of bare Zn and $\text{ZnF}_2@\text{In}@\text{Zn}$ symmetric cells at (a) $5 \text{ mA cm}^{-2}/2 \text{ mAh cm}^{-2}$ and (b) $10 \text{ mA cm}^{-2}/5 \text{ mAh cm}^{-2}$. (c) Comparison of this work with published work on cycle stability of symmetric cells.^{34,41–46} (d) EIS of the $\text{ZnF}_2@\text{In}@\text{Zn}$ symmetric cell at different temperatures. (e) Arrhenius curve and activation energy of bare Zn and $\text{ZnF}_2@\text{In}@\text{Zn}$ anodes based on R_{ct} . (f) Binding models and energies for Zn^{2+} binding to H_2O and ZnF_2 . (g) Adsorption models and energies of zinc atoms with (100)_{Zn}, (002)_{Zn} and (101)_{In} planes.

faster Zn^{2+} transport through the ZnF_2 layer (Fig. S19). Moreover, the (101)_{In} plane has a higher adsorption energy for zinc atoms (-0.42 eV) than the (002)_{Zn} (-0.13 eV) and (100)_{Zn} (-0.23 eV) planes, indicating that the In layer can speed up electrocrystallization of zinc (Fig. 5g). In summary, the faster desolvation of $\text{Zn}(\text{H}_2\text{O})_6^{2+}$, Zn^{2+} transport, and electrocrystallization processes give the $\text{ZnF}_2@\text{In}@\text{Zn}$ anode quicker deposition kinetics than bare Zn, resulting in lower nucleation potential and polarization voltage.

High cycle stability is closely related to uniformity of zinc deposition. When a fixed voltage is applied, a sustained increase in current density over time signifies 2D diffusion,

which is prone to dendrite formation. In contrast, the stabilization of current density after an initial increase indicates 3D diffusion, suggesting uniform zinc deposition. The $\text{ZnF}_2@\text{In}@\text{Zn}$ and $\text{ZnF}_2@\text{Zn}$ anodes transition to 3D diffusion shortly after the initial 2D diffusion ($\sim 2 \text{ s}$), indicating uniform zinc deposition (Fig. S20). Conversely, the $\text{In}@\text{Zn}$ anode and bare Zn show continuous 2D diffusion, implying dendrite formation (Fig. S20).

Fig. S21 presents the cyclic voltammetry (CV) curves for bare Zn and $\text{ZnF}_2@\text{In}@\text{Zn}$ symmetric cells. Compared to bare Zn, the $\text{ZnF}_2@\text{In}@\text{Zn}$ symmetric cell achieves a higher current density as voltage increases, indicative of faster electrochemical



kinetics. The voltage sweep from 0 V to 0.15 V is labeled as step 1, and the reverse sweep from 0.15 V to 0 V is step 2. For the bare Zn symmetric cell, the step 2 current density (i_2) is more than the step 1 current density (i_1) (Fig. S21a). According to the polarization overpotential eqn (4), when the voltage is constant, the limiting current density (i_{lim2}) should be more than the i_{lim1} . According to the relationship between the i_{lim} and the diffusion distance (δ) formula (5), the δ_2 is shorter than δ_1 , indicating the formation of dendrites on the bare Zn surface. In contrast, for the ZnF₂@In@Zn symmetric cell, the current densities in steps 1 and 2 are nearly identical, suggesting uniform zinc deposition (Fig. S21b). Moreover, the crystal surface specific energy will affect the current density. In the ZnF₂@In@Zn symmetric cell, the current densities in steps 1 and 2 are nearly identical, which also reflects the stable surface energy, which is conducive to uniform deposition.

$$\eta_{conc} = \frac{RT}{nF} \ln \left(1 - \frac{i}{i_{lim}} \right) \quad (4)$$

$$i_{lim} = \frac{nFDC_0}{\delta} \quad (5)$$

The (101)_{Zn} plane is known for its lower lattice distortion rate and smaller distortion surface energy change.^{47,48} Under the condition of 1 mA cm⁻²/1 mAh cm⁻², after 25 cycles, ZnF₂@In@Zn shows a higher specific intensity (~9.60) of (101) relative to the sum of (002) and (100) (Fig. S22), compared to (6.87) before cycling (Fig. S6a). This indicates that zinc grows along the (101) plane and increases its exposure. Conversely, bare Zn exhibits a reduced specific intensity (~2.25) (Fig. S22), which can lead to lattice distortion and uneven surface energy distribution, resulting in dendrite growth.

Confocal laser scanning microscopy (CLSM) was used to analyze the surface roughness (S_a) of the anode. Under 1 mA cm⁻²/1 mAh cm⁻² conditions after 25 cycles, the ZnF₂@In@Zn anode shows lower surface roughness ($S_a = 1.71$) than bare Zn ($S_a = 3.09$), indicating more uniform deposition (Fig. 6a and b). Additionally, the height profile of ZnF₂@In@Zn exhibits smaller fluctuations than bare Zn, further confirming its uniform deposition (Fig. S23). SEM reveals the morphological evolution at varying deposition amounts. For bare Zn with a deposition of 0.5 mAh cm⁻², the surface shows small particle accumulation (Fig. 6c). As the deposition increased to 5 mAh cm⁻², particle accumulation became more pronounced, with some areas showing no zinc deposition (Fig. 6d). In contrast, the ZnF₂@In@Zn anode with a deposition of 0.5 mAh cm⁻² displays a uniform distribution of hexagonal zinc particles (Fig. 6e). When the deposition increased to 5 mAh cm⁻², these particles merge into a more uniform surface, indicating that they coalesced during deposition (Fig. 6f). Moreover, mapping and the EDS results of the ZnF₂@In@Zn anode with a deposition amount of 5 mAh cm⁻² show that F remains evenly distributed, whereas In is almost undetectable (Fig. S24). This suggests that zinc deposition occurred between the In layer and the ZnF₂ layer, inhibiting corrosion of the deposited zinc. Optical microscopy further revealed the morphological

evolution of zinc during deposition. For bare Zn, as deposition progressed, noticeable surface protrusions formed, along with bubble formation (Fig. S25a), which indicates dendrite growth and corrosion. Conversely, the ZnF₂@In@Zn anode shows relatively uniform surface deposition with no bubble formation (Fig. S25b).

COMSOL Multiphysics was used to analyze the distributions of current density and Zn²⁺ concentration on the anode surface during deposition. For the bare Zn, uneven passivation layers cause localized deposition. Areas with localized deposition show high current density, whereas the passivation zones (orange) have low current density, worsening zinc deposition unevenness (Fig. 6g). As deposition becomes more uneven, so does the current density distribution. Throughout the deposition process of bare Zn, Zn²⁺ tend to gather at surface protrusions with larger specific surface areas (Fig. S26a). For the ZnF₂@In@Zn anode, the current density stays uniform during deposition (Fig. 6h). In the field of Zn²⁺ concentration, the ZnF₂ layer (yellow) ensures uniform Zn²⁺ distribution, promoting uniform zinc deposition on the In layer (olive green) (Fig. S26b).

To evaluate the impact of the ZnF₂@In@Zn anode on the charge/discharge performance of the cathode, a full cell with NH₄V₄O₁₀ as the cathode (NHVO) is assembled. Given that the NHVO cathode undergoes structural changes during the first cycle, the second cycle of the cyclic voltammetry (CV) curve is analyzed. The ZnF₂@In@Zn/NHVO full cell exhibits lower oxidation peak potentials (1.054 V and 0.758 V) compared to the bare Zn/NHVO full cell (1.097 V and 0.771 V), attributed to its smaller polarization voltage (Fig. 7a). Meanwhile, the reduction peak potential of the ZnF₂@In@Zn/NHVO full cell increases from 0.595 V (bare Zn/NHVO full cells) to 0.604 V, indicating improved full cell energy efficiency (Fig. 7a).

Fig. S27 presents the equivalent circuit diagram of the Zn//NHVO full cell, and Table S2 lists the values of solution resistance (R_s), solid electrolyte interfacial impedance (R_{EIS}), and charge transfer impedance (R_{ct}) for various anodes at different resting times. Electrochemical impedance measurements of the ZnF₂@In@Zn/NHVO full cell at various voltages reveal that the R_{ct} of the ZnF₂@In@Zn anode remains stable throughout discharging (Fig. 7b). However, the ion transport rate declines with decreasing voltage, primarily due to Zn²⁺ embedding in the cathode, hindering Zn²⁺ transport (Fig. 7b). Bare Zn suffers from inert products caused by side reactions, leading to slower surface ion migration (Fig. 7c). During the discharge process, the R_{ct} drops sharply when internal uncorroded Zn is exposed, accelerating the ion transport. Nevertheless, the R_{ct} of the ZnF₂@In@Zn/NHVO full cell remains lower than that of the bare Zn/NHVO full cell. During charging, the ZnF₂@In@Zn/NHVO full cell also demonstrates higher ion migration ability and lower R_{ct} than the bare Zn/NHVO full cell, which results in superior rate performance (Fig. S28). At low current density, the NHVO cathode is not fully activated, making the ion transport on the cathode surface the rate-controlling step, so no significant capacity improvement of the ZnF₂@In@Zn/NHVO full cell is observed. Once activated at low current, the benefits of high ion migration ability and low R_{ct} enhance high-current-density



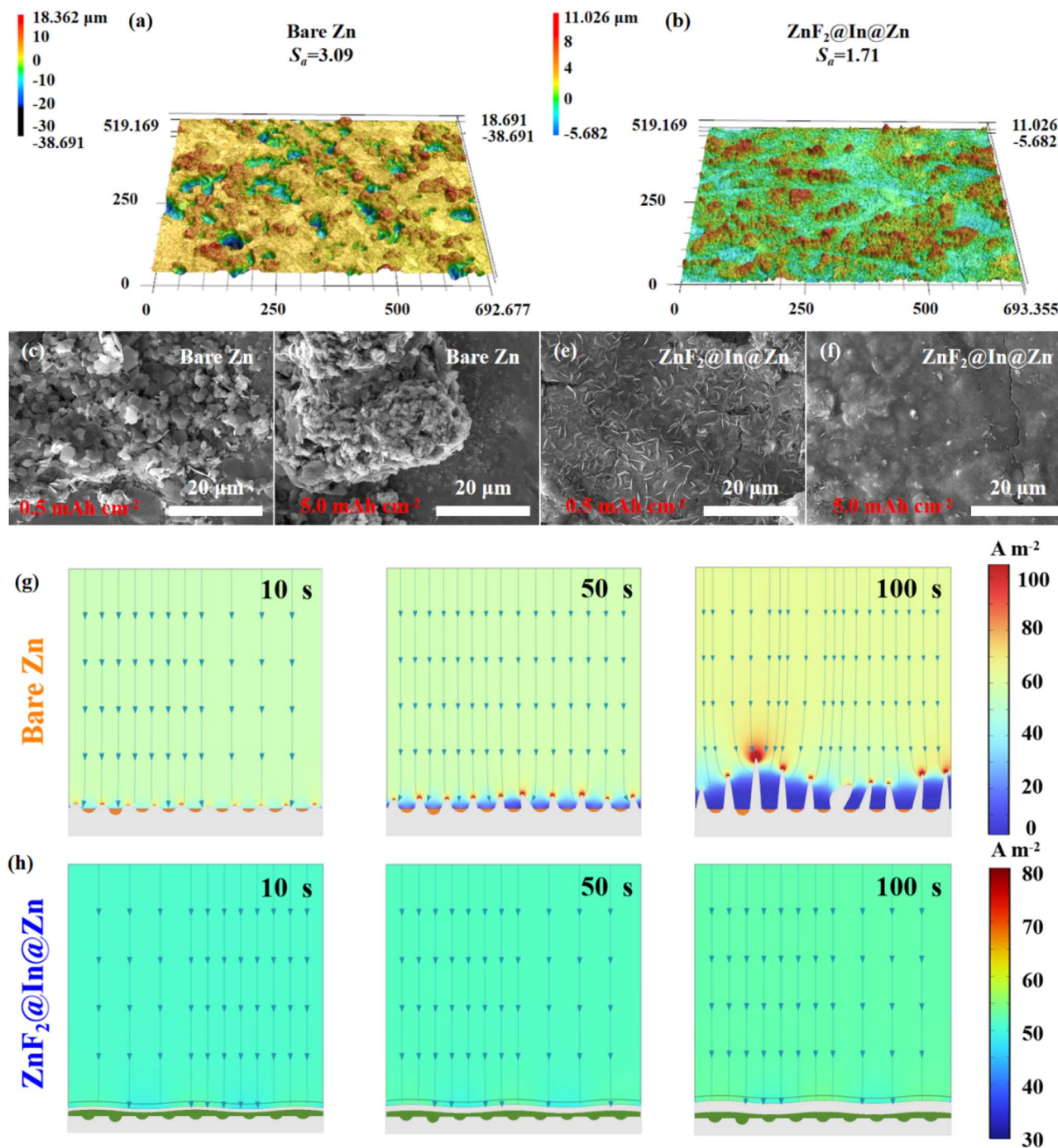


Fig. 6 Study of anode deposition behavior. CLSM images of (a) bare Zn and (b) $\text{ZnF}_2@\text{In}@\text{Zn}$ anodes after 25 cycles at $1 \text{ mA cm}^{-2}/1 \text{ mAh cm}^{-2}$. SEM images of (c and d) bare Zn and (e and f) $\text{ZnF}_2@\text{In}@\text{Zn}$ anodes deposited with (c and e) 0.5 mAh cm^{-2} and (d and f) 5 mAh cm^{-2} after 25 cycles at $1 \text{ mA cm}^{-2}/1 \text{ mAh cm}^{-2}$. Current density profiles of (g) bare Zn and (h) $\text{ZnF}_2@\text{In}@\text{Zn}$ anode surfaces in different deposition states.

performance, giving the $\text{ZnF}_2@\text{In}@\text{Zn}/\text{NHVO}$ full cell a higher capacity (Fig. 7d). Upon returning to low current density, the $\text{ZnF}_2@\text{In}@\text{Zn}/\text{NHVO}$ full cell maintains higher capacity compared to the bare Zn/ NHVO full cell. In addition, the same phenomenon also occurred in $\text{In}@\text{Zn}$ and $\text{ZnF}_2@\text{Zn}$ anodes. At high current densities, full cells assembled with $\text{In}@\text{Zn}$ and $\text{ZnF}_2@\text{Zn}$ anodes also exhibit higher capacity compared to bare Zn (Fig. 7d and S29). Thanks to its ability to

suppress dendrites and corrosion, the $\text{ZnF}_2@\text{In}@\text{Zn}/\text{NHVO}$ full cell retains a capacity of 112.4 mAh g^{-1} after 10 000 cycles at 3 A g^{-1} , corresponding to a capacity retention rate of 79.5% (Fig. 7e and S30). In contrast, the capacity of the bare Zn/ NHVO full cell approaches 0 mAh g^{-1} after 10 000 cycles at 3 A g^{-1} , possibly due to the accumulation of inert products on the anode and cathode (Fig. 7e and S30).



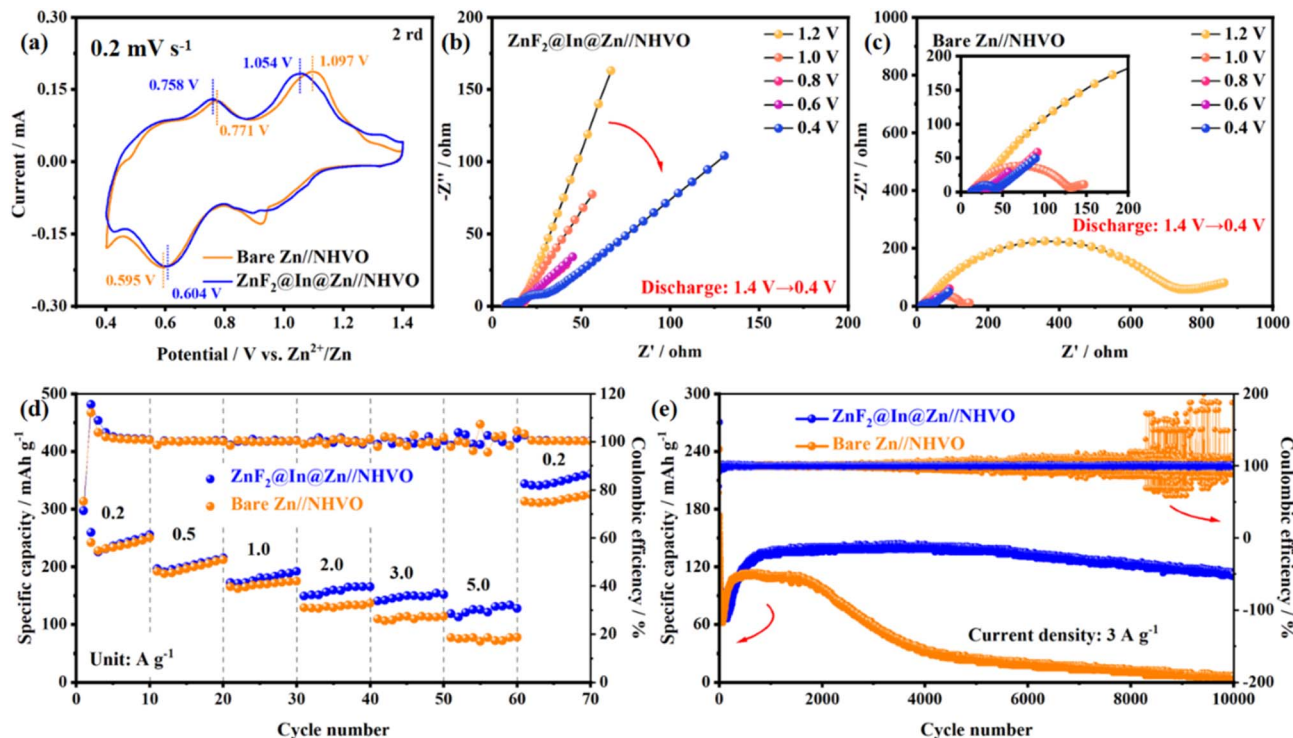


Fig. 7 Study of the Zn//NHVO full cell performance. (a) CV curve of bare Zn//NHVO and $\text{ZnF}_2@\text{In}@\text{Zn}/\text{NHVO}$ full cells. *In situ* EIS spectra of (b) bare Zn//NHVO and (c) $\text{ZnF}_2@\text{In}@\text{Zn}/\text{NHVO}$ full cells discharged from 1.4 V to 0.4 V. (d) Rate and (e) cycle performance of the Zn//NHVO full cell.

3 Conclusion

In summary, we have introduced a novel leveling–shielding dual strategy to enhance the performance of zinc anodes. The low-melting-point In metal serves as a leveling agent to repair surface defects due to the decomposition of $\text{Zn}_2(\text{OH})_2\text{CO}_3$ during heat treatment and induces uniform and rapid zinc deposition by exposing a single (101)_{In} plane. The outermost ZnF_2 layer not only suppresses the corrosion of deposited zinc but also accelerates the de-solvation process of $\text{Zn}(\text{H}_2\text{O})_6^{2+}$, thereby improving electrochemical reaction kinetics. Therefore, the $\text{ZnF}_2@\text{In}@\text{Zn}$ symmetric cell demonstrates exceptional performance, achieving an ultra-low interfacial impedance of less than 10 Ω and stable cycling for over 2800 h with a polarization voltage of 21.8 mV at 5 mA cm^{-2} and 2 mAh cm^{-2} , which is a significant improvement over bare Zn (140 h and 75.8 mV). Additionally, the $\text{ZnF}_2@\text{In}@\text{Zn}/\text{NH}_4\text{V}_4\text{O}_{10}$ full cell exhibits remarkable long-term stability, retaining a capacity of 112.4 mAh g^{-1} after 10 000 cycles at 3 A g^{-1} , corresponding to a capacity retention rate of 79.5%. Our findings demonstrate that this leveling–shielding dual strategy effectively addresses critical issues such as dendrite formation and corrosion in aqueous zinc ion batteries at no cost to energy efficiency, while providing a promising route for addressing similar issues in other metal anodes.

Author contributions

Qing Wen is responsible for completing most of the experiments, data analysis and article writing. Taixu Hao is

responsible for DFT calculations and COMSOL Multiphysics. Tian Chen, Dinghao Le and Pei Yang are responsible for electrochemical performance testing and analysis. Hezhang Chen and Linbo Tang are responsible for XRD and SEM analysis. Qing Wu provided a platform for simulation calculations. Xiahui Zhang and Junchao Zheng are responsible for paper guidance and revision.

Conflicts of interest

The authors declare that they have no conflict of interest.

Data availability

The data that support the findings of this study are available from the corresponding author, Junchao Zheng, jczheng@csu.edu.cn, upon reasonable request.

The supplementary information file contains includes experimental methods, figures, tables, and extended analyses to support data reproducibility and interpretation. See DOI: <https://doi.org/10.1039/d5sc04875c>.

Acknowledgements

This work was supported in part by the High Performance Computing Center of Central South University. We gratefully acknowledge the financial support from the National Natural Science Foundation of China (52272261), the Science and Technology Innovation Program of Hunan Province



(2024RC1021), the Hunan Provincial Natural Science Foundation of China (2024JJ4062), the Department of Education of Hunan Province of China (23B0020), and the Science and Technology Program of Changsha City (kq2402211).

References

- M. Khalid, Smart grids and renewable energy systems: Perspectives and grid integration challenges, *Energy Strategy Rev.*, 2024, **51**, 101299.
- W. Chen, M. Alharthi, J. J. Zhang and I. Khan, The need for energy efficiency and economic prosperity in a sustainable environment, *Gondwana Res.*, 2024, **127**, 22–35.
- F. Vidal, E. R. van der Marel, R. W. F. Kerr, C. McElroy, N. Schroeder, C. Mitchell, G. Rosetto, T. T. D. Chen, R. M. Bailey, C. Hepburn, *et al.*, Designing a circular carbon and plastics economy for a sustainable future, *Nature*, 2024, **626**(7997), 45–57.
- Y. Y. Jiang, S. M. Sun, R. J. Xu, F. Liu, X. D. Miao, G. L. Ran, K. R. Liu, Y. P. Yi, W. K. Zhang and X. Z. Zhu, Non-fullerene acceptor with asymmetric structure and phenyl-substituted alkyl side chain for 20.2% efficiency organic solar cells, *Nat. Energy*, 2024, **9**(8), 975–986.
- Q. Hassan, P. Viktor, T. J. Al-Musawi, B. M. Ali, S. Algburi, H. M. Alzoubi, A. K. Al-Jiboory, A. Z. Sameen, H. M. Salman and M. Jaszczur, The renewable energy role in the global energy Transformations, *Renew. Energy Focus*, 2024, **48**, 100545.
- L. Zhang, C. Zhang and E. J. Berg, Mastering Proton Activities in Aqueous Batteries, *Adv. Mater.*, 2025, **37**(23), 2407852.
- X. H. Yi, H. W. Fu, A. M. Rao, Y. J. Zhang, J. Zhou, C. X. Wang and B. G. Lu, Safe electrolyte for long-cycling alkali-ion batteries, *Nat Sustainability*, 2024, **7**(3), 326–337.
- C. Y. Zhu, M. X. Wang, M. X. Guo, J. X. Deng, Q. P. Du, W. Wei, Y. X. Zhang and S. S. A. Talesh, Optimizing solar-driven multi-generation systems: A cascade heat recovery approach for power, cooling, and freshwater production, *Appl. Therm. Eng.*, 2024, **240**, 122214.
- X. Shi, J. H. Xie, J. Wang, S. L. Xie, Z. J. Yang and X. H. Lu, A weakly solvating electrolyte towards practical rechargeable aqueous zinc-ion batteries, *Nat. Commun.*, 2024, **15**(1), 302.
- X. Y. Dou, X. F. Xie, S. Q. Liang and G. Z. Fang, Low-current-density stability of vanadium-based cathodes for aqueous zinc-ion batteries, *Sci. Bull.*, 2024, **69**(6), 833–845.
- L. P. Wang, B. Zhang, W. H. Zhou, Z. W. Zhao, X. Liu, R. Z. Zhao, Z. H. Sun, H. P. Li, X. Wang, T. S. Zhang, *et al.*, Tandem Chemistry with Janus Mesopores Accelerator for Efficient Aqueous Batteries, *J. Am. Chem. Soc.*, 2024, **146**(9), 6199–6208.
- V. Vanoppen, L. Zhang, E. J. Berg and X. Hou, Manipulating Horizontal Zn Deposition with Indium Salt Additive for Anode-Free Zn Batteries, *ACS Mater. Lett.*, 2024, **6**(11), 4881–4888.
- M. He, C. Z. Shu, A. J. Hu, R. X. Zheng, M. L. Li, Z. Q. Ran and J. P. Long, Suppressing dendrite growth and side reactions on Zn metal anode via guiding interfacial anion/cation/H₂O distribution by artificial multi-functional interface layer, *Energy Storage Mater.*, 2022, **44**, 452–460.
- Y. X. Lin, Z. X. Mai, H. K. Liang, Y. Li, G. Z. Yang and C. X. Wang, Dendrite-free Zn anode enabled by anionic surfactant-induced horizontal growth for highly-stable aqueous Zn-ion pouch cells, *Energy Environ. Sci.*, 2023, **16**(2), 687–697.
- S. L. Liu, J. F. Mao, W. K. Pang, J. Vongsivut, X. H. Zeng, L. Thomsen, Y. Y. Wang, J. W. Liu, D. Li and Z. P. Guo, Tuning the Electrolyte Solvation Structure to Suppress Cathode Dissolution, Water Reactivity, and Zn Dendrite Growth in Zinc-Ion Batteries, *Adv. Funct. Mater.*, 2021, **31**(38), 2104281.
- M. Zhou, S. Guo, J. L. Li, X. B. Luo, Z. X. Liu, T. S. Zhang, X. X. Cao, M. Q. Long, B. G. Lu, A. Q. Pan, *et al.*, Surface-Preferred Crystal Plane for a Stable and Reversible Zinc Anode, *Adv. Mater.*, 2021, **33**(21), 2100187.
- H. Fu, L. Xiong, W. Han, M. Wang, Y. J. Kim, X. Y. Li, W. Yang and G. Liu, Highly active crystal planes-oriented texture for reversible high-performance Zn metal batteries, *Energy Storage Mater.*, 2022, **51**, 550–558.
- T. Wang, J. M. Sun, Y. B. Hua, B. N. V. Krishna, Q. Xi, W. Ai and J. S. Yu, Planar and dendrite-free zinc deposition enabled by exposed crystal plane optimization of zinc anode, *Energy Storage Mater.*, 2022, **53**, 273–304.
- Z. X. Liu, R. Wang, Q. W. Ma, J. D. Wan, S. L. Zhang, L. H. Zhang, H. B. Li, Q. Q. Luo, J. Wu, T. F. Zhou, *et al.*, A Dual-Functional Organic Electrolyte Additive with Regulating Suitable Overpotential for Building Highly Reversible Aqueous Zinc Ion Batteries, *Adv. Funct. Mater.*, 2024, **34**(5), 2214538.
- Q. Z. Gou, H. R. Luo, Q. Zhang, J. B. Deng, R. Z. Zhao, O. Odunmbaku, L. Wang, L. J. Li, Y. J. Zheng, J. Li, *et al.*, Electrolyte Regulation of Bio-Inspired Zincophilic Additive toward High-Performance Dendrite-Free Aqueous Zinc-Ion Batteries, *Small*, 2023, **19**(10), 2207502.
- L. P. Li, S. L. Liu, W. C. Liu, D. L. Ba, W. Y. Liu, Q. Y. Gui, Y. Chen, Z. Q. Hu, Y. Y. Li and J. P. Liu, Electrolyte Concentration Regulation Boosting Zinc Storage Stability of High-Capacity K_{0.486}V₂O₅ Cathode for Bendable Quasi-Solid-State Zinc Ion Batteries, *Nano-Micro Lett.*, 2021, **13**(1), 34.
- J. Q. Huang, X. W. Chi, J. Wu, J. J. Liu and Y. Liu, High-concentration dual-complex electrolyte enabled a neutral aqueous zinc-manganese electrolytic battery with superior stability, *Chem. Eng. J.*, 2022, **430**, 133058.
- Z. F. Wang, H. F. Li, Z. J. Tang, Z. X. Liu, Z. H. Ruan, L. T. Ma, Q. Yang, D. H. Wang and C. Y. Zhi, Hydrogel Electrolytes for Flexible Aqueous Energy Storage Devices, *Adv. Funct. Mater.*, 2018, **28**(48), 1804560.
- F. N. Mo, Z. Chen, G. J. Liang, D. H. Wang, Y. W. Zhao, H. F. Li, B. B. Dong and C. Y. Zhi, Zwitterionic Sulfobetaine Hydrogel Electrolyte Building Separated Positive/Negative Ion Migration Channels for Aqueous Zn-MnO₂ Batteries with Superior Rate Capabilities, *Adv. Energy Mater.*, 2020, **10**(16), 2000035.



- 25 J. R. Wang, L. Szabo, D. Madhav, I. Ferreira and V. Vandeginste, Recent progress in interfacial engineering strategies for Mn-based oxide cathodes in aqueous zinc-ion batteries: Mechanisms, modifications, and performance enhancement, *Energy Storage Mater.*, 2023, **63**, 103015.
- 26 Q. Wen, H. Fu, R. D. Cui, H. Z. Chen, R. H. Ji, L. B. Tang, C. Yan, J. Mao, K. H. Dai, X. H. Zhang, *et al.*, Recent advances in interfacial modification of zinc anode for aqueous rechargeable zinc ion batteries, *J. Energy Chem.*, 2023, **83**, 287–303.
- 27 D. L. Han, S. C. Wu, S. W. Zhang, Y. Q. Deng, C. J. Cui, L. A. Zhang, Y. Long, H. Li, Y. Tao, Z. Weng, *et al.*, A Corrosion-Resistant and Dendrite-Free Zinc Metal Anode in Aqueous Systems, *Small*, 2020, **16**(29), 2001736.
- 28 Z. Cai, Y. T. Ou, J. D. Wang, R. Xiao, L. Fu, Z. Yuan, R. M. Zhan and Y. M. Sun, Chemically resistant Cu-Zn/Zn composite anode for long cycling aqueous batteries, *Energy Storage Mater.*, 2020, **27**, 205–211.
- 29 S. Y. Li, J. Fu, G. X. Miao, S. P. Wang, W. Y. Zhao, Z. C. Wu, Y. J. Zhang and X. W. Yang, Toward Planar and Dendrite-Free Zn Electrodepositions by Regulating Sn-Crystal Textured Surface, *Adv. Mater.*, 2021, **33**(21), 2008424.
- 30 J. Han, H. Euchner, M. Kuenzel, S. M. Hosseini, A. Gross, A. Varzi and S. Passerini, A Thin and Uniform Fluoride-Based Artificial Interphase for the Zinc Metal Anode Enabling Reversible Zn/MnO₂ Batteries, *ACS Energy Lett.*, 2021, **6**(9), 3063–3071.
- 31 Y. Yang, G. Qu, Z. Wei, T. Hu, Y. Hu, Z. Wei, F. Mo, H. Li and G. Liang, Constructing a Fluoride-Ion Tunnel-Structured Interface to Stabilize the Zn Metal Chemistry at 50 °C, *Adv. Funct. Mater.*, 2024, **34**(51), 2409950.
- 32 J. Ge, Y. Zhang, Z. Xie, H. Xie, W. Chen and B. Lu, Tailored ZnF₂/ZnS-rich interphase for reversible aqueous Zn batteries, *Nano Res.*, 2023, **16**(4), 4996–5005.
- 33 X. Z. Yang, C. Li, Z. T. Sun, S. Yang, Z. X. Shi, R. Huang, B. Z. Liu, S. Li, Y. H. Wu, M. L. Wang, *et al.*, Interfacial Manipulation via In Situ Grown ZnSe Cultivator toward Highly Reversible Zn Metal Anodes, *Adv. Mater.*, 2021, **33**(52), 2105951.
- 34 D. Guo, F. Li and B. Zhang, Nano-Zinc Sulfide Modified 3D Reconstructed Zinc Anode with Induced Deposition Effect Assists Long-Cycle Stable Aqueous Zinc Ion Battery, *Adv. Sci.*, 2025, **12**(10), 2417323.
- 35 J. Li, Y. Dai, Q. Chen, R. Zheng, Y. Zhao, Z. Wang, H. Sun and Y. Liu, Inorganic-metal hybrid coating for stabilizing and regulating aqueous zinc anodes, *J. Colloid Interface Sci.*, 2025, **687**, 479–488.
- 36 J. Zhou, Y. Mei, F. Wu, Y. Hao, W. Ma, L. Li, M. Xie and R. Chen, Regulated Ion/Electron-Conducting Interphase Enables Stable Zinc-Metal Anodes for Aqueous Zinc-Ions Batteries, *Angew. Chem.*, 2023, **62**(29), e202304454.
- 37 X. S. Xie, S. Q. Liang, J. W. Gao, S. Guo, J. B. Guo, C. Wang, G. Y. Xu, X. W. Wu, G. Chen and J. Zhou, Manipulating the ion-transfer kinetics and interface stability for high-performance zinc metal anodes, *Energy Environ. Sci.*, 2020, **13**(2), 503–510.
- 38 G. Li, X. Wang, S. Lv, J. Wang, W. Yu, X. Dong and D. Liu, In Situ Constructing a Film-Coated 3D Porous Zn Anode by Iodine Etching Strategy Toward Horizontally Arranged Dendrite-Free Zn Deposition, *Adv. Funct. Mater.*, 2023, **33**(4), 2208288.
- 39 Z. Pan, Q. Cao, W. Gong, J. Yang, Y. Gao, Y. Gao, J. Pu, J. Sun, X. J. Loh, Z. Liu, *et al.*, Zincophilic 3D ZnOHF nanowire arrays with ordered and continuous Zn²⁺ Ion modulation layer enable long-term stable Zn metal anodes, *Energy Storage Mater.*, 2022, **50**, 435–443.
- 40 G. Ma, K. Chen, H. Qiao, J. Liu, H. Dong and Y. Gao, Porous V₂CT_x MXene as a High Stability Zinc Anode Protective Coating, *Nano Lett.*, 2024, **24**(46), 14552–14558.
- 41 M. Zhu, H. Wang, H. Wang, C. Li, D. Chen, K. Wang, Z. Bai, S. Chen, Y. Zhang and Y. Tang, A Fluorinated Solid-state-electrolyte Interface Layer Guiding Fast Zinc-ion Oriented Deposition in Aqueous Zinc-ion Batteries, *Angew. Chem.*, 2024, **63**(4), e202316904.
- 42 F. Zhang, H. Tao, Y. Li and X. Yang, β'-Al₂O₃ protecting layer for stable zinc metal anodes, *Mater. Today Commun.*, 2024, **39**, 108606.
- 43 M. Abouali, S. Adhami, S. A. Haris and R. Yuksel, On the Dendrite-Suppressing Effect of Laser-Processed Polylactic Acid-Derived Carbon Coated Zinc Anode in Aqueous Zinc Ion Batteries, *Angew. Chem.*, 2024, **63**(28), e202405048.
- 44 X. Wang, Y. Tian, K. Yang, C. Ma, W. Lu, X. Bian, N. Chen, H. Jiang, Y. Li, X. Meng, *et al.*, Sandwich-structured anode enables high stability and enhanced zinc utilization for aqueous Zn-ion batteries, *Energy Storage Mater.*, 2024, **64**, 103078.
- 45 X. Yu, T. Zhang, D. Yu, T. Tian, H. Niu, W. Yang and D. Sun, Stabilizing Zn anodes via a binder-free MoS₂ interface with charge regulation toward stable Zinc-Ion batteries, *Chem. Eng. Sci.*, 2024, **299**, 120523.
- 46 Q. Wen, H. Fu, C. Sun, R. Cui, H. Chen, R. Ji, L. Tang, L. Li, J. Wang, Q. Wu, *et al.*, Buried interface engineering towards stable zinc anodes for high-performance aqueous zinc-ion batteries, *Sci. Bull.*, 2025, **70**(4), 518–528.
- 47 Z. P. Liu, Z. K. Guo, L. S. Fan, C. Y. Zhao, A. S. Chen, M. Wang, M. Li, X. Y. Lu, J. C. Zhang, Y. Zhang, *et al.*, Construct Robust Epitaxial Growth of (101) Textured Zinc Metal Anode for Long Life and High Capacity in Mild Aqueous Zinc-Ion Batteries, *Adv. Mater.*, 2024, **36**(5), 2305988.
- 48 Y. Y. Wang, J. X. Lv, L. X. Hong, J. K. Zhang, C. X. Chen, A. Xu, M. Huang, X. B. Ren, J. B. Bai, H. Wang, *et al.*, Customizing H₂O-Poor Electric Double Layer and Boosting Texture Exposure of Zn (101) Plane towards Super-High Areal Capacity Zinc Metal Batteries, *Angew. Chem.*, 2025, **64**(2), e202414757.

